Robust Electrical Impedance Tomography via Half-Quadratic Optimization

Min Duan, Xiao-Peng Li, *Member, IEEE*, Jia-Xin Chen, Lin Yang, and Meng Dai

***Abstract*—Electrical impedance tomography (EIT) is a promising imaging technique in the medical field. However, its clinical application is limited by several challenges, such as poor electrode contact and body movement. These factors introduce impulsive noise in boundary voltage measurement, resulting in the performance degradation of the conventional imaging methods. This letter devises a robust approach to improve the performance in such scenarios. Unlike traditional algorithms that use an identity matrix as the measurement noise weight matrix, the suggested method designs a strategy to update the weight matrix during iteration for outlier resistance. Specifically, we apply the penalty technique to optimize the weight matrix and thus formulate the imaging task as a half-quadratic optimization problem. In addition, we exploit a median absolute deviation based confidence interval to distinguish outlier-contaminated and normal channels, such that the elements of the diagonal weight matrix are either 0 or 1. Subsequently, the resultant optimization task is addressed using the alternating minimization method. Experimental results show that the proposed approach outperforms the state-of-the-art algorithms in the presence of impulsive noise.**

***Index Terms*—Electrical impedance tomography, impulsive noise, half-quadratic optimization, alternating minimization.**

I. INTRODUCTION

ELECTRICAL impedance tomography (EIT) is a non-invasive imaging technique to reconstruct the internal electrical impedance distribution by measuring voltages on the object surface [1]. It can be applied to several fields, such as medicine [2], [3] and material testing [4], [5]. In medicine, it has been used to lung ventilation monitoring, brain activity monitoring, and respiratory disease diagnosis [6], [7], [8], [9], [10]. Compared with magnetic resonance imaging (MRI) [11] and computed tomography (CT) [12], EIT allows for real-time dynamic imaging and makes the equipment ideal for bedside use in intensive care units.

In the past decades, researchers have proposed different techniques for EIT imaging, including least squares method [13], [14], Bayesian approach [15], [16], [17], and deep learning strategy [18], [19]. Works [13], [14] formulated the imaging task as a linear regression problem with a Tikhonov regularization term. Compared with [13], [14] modified the regularizer to improve the imaging performance. In [15], [16], Liu et al. employed the structure-aware sparse Bayesian learning (SA-SBL) approach to reconstruct EIT images. As they exploit the prior knowledge of practical conductivity distribution, the imaging performance is significantly improved. Besides, Liu et al. extended SA-SBL to frequency-difference EIT (fdEIT) problem [17]. In contrast to EIT, fdEIT is able to mitigate the systematic artifacts induced by modeling errors when a baseline dataset is unavailable. In [18], Liu et al. utilized the deep image prior neutral network to reconstruct EIT images. Furthermore, Yang et al. combined supervised and unsupervised learning to design the neural network structure, ensuring adherence to the underlying physical laws [19].

During EIT voltage acquisition, body movement and poor electrode contact are inevitable, generating impulsive noise in measurements [20]. As the ℓ_2-norm is sensitive to outliers, the ℓ_2-norm based methods appear performance deterioration in such scenarios. To address this issue, Borsic and Adler employed the ℓ_1-norm to reformulate the imaging task and thus the corresponding algorithm is robust to impulsive noise [21].

However, the ℓ_1-norm based method cannot obtain the optimal solution in the presence of impulsive noise. This is because the entry-wise ℓ_1-norm assumes that all channels of EIT boundary voltages contain impulsive noise, while partial channels are affected by outliers in practice.

To resist impulsive noise, this letter devises a robust EIT approach via dynamically updating the measurement noise weight matrix. Our contributions are summarized as follows:

- *Novel strategy to update weight matrix:* We introduce a regularization term for the weight matrix to reformulate the imaging task as a HQ optimization problem [22]. In doing so, we improve the imaging performance in impulsive-noise environment.
- *Efficient method:* Although the performance of our algorithm depends on an auxiliary variable, we provide an adaptive manner to determine it. Specifically, its value is updated using a MAD based confidence interval to identify the channels corrupted by outliers.
- *Enhanced EIT imaging performance:* We conduct experiments using resistor-net and clinical data to demonstrate the superiority of the proposed method over the conventional approaches in the presence of impulsive noise.

Received 26 April 2025; revised 13 July 2025; accepted 21 July 2025. Date of publication 24 July 2025; date of current version 4 August 2025. This work was supported in part by the National Natural Science Foundation of China under Grant 62401373 and Grant 52277235, in part by the Young Innovative Talents Project of Guangdong Provincial Department of Education (Natural Science), China under Grant 2023KQNCX063, and in part by the 2035 Excellence Pursuit Plan Level B of Shenzhen University under Grant 2022B009. The associate editor coordinating the review of this article and approving it for publication was Dr. Federico Fontana. *(Corresponding authors: Xiao-Peng Li; Meng Dai.)*

Min Duan, Xiao-Peng Li, and Jia-Xin Chen are with the State Key Laboratory of Radio Frequency Heterogeneous Integration, Shenzhen University, Shenzhen 518060, China (e-mail: x.p.li@szu.edu.cn).

Lin Yang is with the Department of Aerospace Medicine, Fourth Military Medical University, Xi'an 710032, China.

Meng Dai is with the Department of Biomedical Engineering and Innovation Research Institution, Xijing Hospital, Fourth Military Medical University, Xi'an 710032, China (e-mail: daimeng@fmmu.edu.cn).

Digital Object Identifier 10.1109/LSP.2025.3592596

II. PRELIMINARY

To collect voltages, small current is injected into the body via one pair of electrodes and then the boundary voltages are measured at the other electrode pairs. Subsequently, the measurements are exploited to reconstruct EIT images. Prior to imaging, we require calculating the boundary voltage change $\Delta\boldsymbol{v} = \boldsymbol{v}_{t_2} - \boldsymbol{v}_{t_1} = \Delta\tilde{\boldsymbol{v}} + \boldsymbol{n}$, where $\boldsymbol{v}_{t_1} \in \mathbb{R}^m$ and $\boldsymbol{v}_{t_2} \in \mathbb{R}^m$ represent the boundary voltages at time-slot t_1 and t_2, respectively, $\Delta\tilde{\boldsymbol{v}} \in \mathbb{R}^m$ is the noise-free boundary voltage change, and $\boldsymbol{n} \in \mathbb{R}^m$ denotes the noise vector.

Then, the relationship between the boundary voltage change $\Delta\boldsymbol{v}$ and the conductivity change $\Delta\boldsymbol{\rho} \in \mathbb{R}^n$ can be modeled as $\Delta\boldsymbol{v} = \boldsymbol{J}\Delta\boldsymbol{\rho} + \boldsymbol{n}$, where $\boldsymbol{J} \in \mathbb{R}^{m\times n}$ is the known Jacobian matrix [23].

Under an assumption that $\boldsymbol{n}$ obeys the zero-mean Gaussian distribution, the optimization problem for the conductivity change is formulated as

$$\min_{\Delta\boldsymbol{\rho}} \|\sqrt{\boldsymbol{W}}(\Delta\boldsymbol{v} - \boldsymbol{J}\Delta\boldsymbol{\rho})\|_2^2 + \lambda\|\sqrt{\boldsymbol{Q}}\Delta\boldsymbol{\rho}\|_2^2, \tag{1}$$

where $\|\cdot\|_2$ denotes the ℓ_2-norm, $\lambda > 0$ is a penalty parameter, while $\boldsymbol{W} \in \mathbb{R}^{m\times m}$ and $\boldsymbol{Q} \in \mathbb{R}^{n\times n}$ are calculated by $\boldsymbol{W} = (\boldsymbol{\Sigma}_n)^{-1} = \frac{1}{\sigma_n^2}\boldsymbol{I}$ and $\boldsymbol{Q} = (\boldsymbol{\Sigma}_t)^{-1}$, respectively. Herein, $\boldsymbol{\Sigma}_n$ is the estimated noise covariance and $\boldsymbol{\Sigma}_t$ denotes the effective covariance of the training targets.

As (1) is a linear least squares problem with an ℓ_2-norm regularization term, its closed-form optimal solution is $\Delta\boldsymbol{\rho}^* = (\boldsymbol{J}^{\mathrm{T}}\boldsymbol{W}\boldsymbol{J} + \lambda\boldsymbol{Q})^{-1}\boldsymbol{J}^{\mathrm{T}}\boldsymbol{W}\Delta\boldsymbol{v}$, where $(\cdot)^{\mathrm{T}}$ denotes the transpose operator. Finally, $\Delta\boldsymbol{\rho}^*$ is reshaped to obtain an EIT image.

III. ALGORITHM DEVELOPMENT

In this section, the proposed algorithm, its convergence analysis, and computational complexity are presented.

A. Proposed Algorithm

To eliminate the influence of outliers on $\Delta\boldsymbol{\rho}$, we introduce a regularization term $\mathcal{L}_a(\cdot)$ to update the diagonal weight matrix $\boldsymbol{W}$, resulting in

$$\begin{aligned}\mathcal{H}(\Delta\boldsymbol{\rho}, \boldsymbol{W}) = \min_{\boldsymbol{W},\Delta\boldsymbol{\rho}} \ & \frac{1}{2}\|\sqrt{\boldsymbol{W}}(\Delta\boldsymbol{v} - \boldsymbol{J}\Delta\boldsymbol{\rho})\|_2^2 + \mathcal{L}_a(\boldsymbol{W}) \\ & + \lambda\|\sqrt{\boldsymbol{Q}}\Delta\boldsymbol{\rho}\|_2^2,\end{aligned} \tag{2}$$

where $\mathcal{L}_a(\cdot)$ is an element-wise function, defined as

$$\mathcal{L}_a(w) = \begin{cases} \frac{1-w}{2}a^2, & 0 \le w < 1, \\ 0, & w \ge 1, \end{cases} \tag{3}$$

where $a > 0$ and the derivation of $\mathcal{L}_a(\cdot)$ is elaborated in the next subsection.

As (2) has two variables, AM is adopted as the solver, leading to

$$\Delta\boldsymbol{\rho}^{k+1} = \arg\min_{\Delta\boldsymbol{\rho}} \frac{1}{2}\|\sqrt{\boldsymbol{W}^k}(\Delta\boldsymbol{v} - \boldsymbol{J}\Delta\boldsymbol{\rho})\|_2^2 + \lambda\|\sqrt{\boldsymbol{Q}}\Delta\boldsymbol{\rho}\|_2^2, \tag{4a}$$

$$\boldsymbol{W}^{k+1} = \operatorname*{argmin}_{\boldsymbol{W}} \frac{1}{2}\|\sqrt{\boldsymbol{W}}\left(\Delta\boldsymbol{v} - \boldsymbol{J}\Delta\boldsymbol{\rho}^{k+1}\right)\|_2^2 + \mathcal{L}_a(\boldsymbol{W}). \tag{4b}$$

Algorithm 1: REIT-HQ.

```
**Input:** $\Delta\boldsymbol{v} \in \mathbb{R}^{192}$, $\boldsymbol{J} \in \mathbb{R}^{192\times 623}$, $\boldsymbol{Q} \in \mathbb{R}^{623\times 623}$,
$\eta = 1.8$, $\lambda = 0.1$, tol $= 10^{-6}$, and $K_{\text{max}} = 50$.
Initialization: $\boldsymbol{W}^0 = \boldsymbol{I}$
for $k = 1, 2, \ldots, K_{\text{max}}$ do
    1) Update $\Delta\boldsymbol{\rho}^{k+1}$ via (5)
    2) Calculate $a^{k+1}$ as $a^{k+1} = \min\{\eta\sigma^{k+1}, a^k\}$
    3) Update $\boldsymbol{W}^{k+1}$ via (6c)
    Stop if $\|\Delta\boldsymbol{\rho}^{k+1} - \Delta\boldsymbol{\rho}^k\|_2 \le$ tol
end for
Output: $\Delta\boldsymbol{\rho}^*$
```

For (4a), it is same to (1) and thus its optimal solution is

$$\Delta\boldsymbol{\rho}^{k+1} = \left(\boldsymbol{J}^{\mathrm{T}}\sqrt{\boldsymbol{W}^k}\boldsymbol{J} + \lambda\boldsymbol{Q}\right)^{-1}\boldsymbol{J}^{\mathrm{T}}\sqrt{\boldsymbol{W}^k}\Delta\boldsymbol{v}. \tag{5}$$

For (4b), we seek for its optimal solution based the following element-wise format:

$$\arg\min_{w_{i,i}} \sum_{i}^{m} \frac{w_{i,i}(e_i^{k+1})^2}{2} + \mathcal{L}_a(w_{i,i}) \tag{6a}$$

$$= \begin{cases} \arg\min\limits_{w_{i,i}} \sum_i^m \frac{w_{i,i}(e_i^{k+1})^2}{2} + \frac{1-w_{i,i}}{2}a^2, 0 \le w_{i,i} < 1, \\ \arg\min\limits_{w_{i,i}} \sum_i^m \frac{w_{i,i}(e_i^{k+1})^2}{2}, \qquad\qquad w_{i,i} > 1 \end{cases} \tag{6b}$$

$$= \begin{cases} 1, & |e_i^{k+1}| \le a, \\ 0, & |e_i^{k+1}| > a, \end{cases} \tag{6c}$$

where $\boldsymbol{e}^{k+1} = \Delta\boldsymbol{v} - \boldsymbol{J}\Delta\boldsymbol{\rho}^{k+1}$ is the fitting error in the $(k+1)$-th iteration. For e_i^{k+1}, a large absolute value signifies that the corresponding i-th channel is corrupted by outliers. Besides, (6c) indicates that if $|e_i^{k+1}|$ is larger than a, the corresponding $w_{i,i}$ is set to 0. As a result, the impact of the outlier-contaminated channel on EIT imaging is weakened. Furthermore, we require an appropriate a to identify the channels corrupted by impulsive noise.

As $[-a, a]$ can be considered as a confidence interval to distinguish the normal entries and outliers, we exploit the MAD method to calculate the standard deviation:

$$\sigma^{k+1} = 1.4826 \times \text{Med}\left(|\boldsymbol{e}^{k+1} - \text{Med}(\boldsymbol{e}^{k+1})|\right), \tag{7}$$

where Med$(\cdot)$ is median operator. Then, we introduce $\eta > 0$ to control the range of the confidence interval, resulting in $a^{k+1} = \eta\sigma$. Moreover, to guarantee the convergence of the proposed method, a is limited by $a^{k+1} = \min\{\eta\sigma^{k+1}, a^k\}$. That is, a^{k+1} is non-decreasing.

The proposed approach is referred to robust EIT via HQ optimization (REIT-HQ), which is summarized in Algorithm 1. After obtaining $\Delta\boldsymbol{\rho}^*$, we can exploit the method in [24] to reshape it into an EIT image with the dimensions of 32×32.

B. Regularization Term Derivation

In this subsection, we detail the expression of $\mathcal{L}_a(\cdot)$. As the main idea to design $\mathcal{L}_a(\cdot)$ is to resist impulsive noise, we construct it based on the robust truncated-quadratic function [25],

[26]

$$\mathcal{F}(e)=\begin{cases}\frac{e^2}{2}, & |e|<a,\\ \frac{a^2}{2}, & |e|\geq a,\end{cases} \tag{8}$$

where $a>0$ can be considered as a threshold. According to HQ optimization, (8) is equivalent to the following problem:

$$\mathcal{F}(e)=\min_{w}\frac{we^2}{2}+\mathcal{J}(w), \tag{9}$$

where w is an auxiliary variable and $\mathcal{J}(w)$ is the *dual function* of $\mathcal{F}(e)$. It is seen that the form of (9) is similar to the element-wise form of (2) w.r.t. $\boldsymbol{W}$. Therefore, $\mathcal{J}(\cdot)$ can be applied to $\mathcal{L}_a(\cdot)$. The derivation of $\mathcal{J}(\cdot)$ is given as follows.

For (9), the multiplicative form of $\mathcal{J}(w)$ is expressed as [22]

$$\mathcal{J}(w)=\mathcal{L}_a(w)=\sup_{e}-\frac{we^2}{2}+\mathcal{F}(e). \tag{10}$$

Then, substituting (8) into (10) yields:

$$\begin{aligned}\mathcal{J}(w)=\mathcal{L}_a(w)&=\begin{cases}\sup\limits_{e}\left(-\frac{we^2}{2}+\frac{e^2}{2}\right), & |e|<a,\\ \sup\limits_{e}\left(-\frac{we^2}{2}+\frac{a^2}{2}\right), & |e|\geq a,\end{cases}\\ &=\begin{cases}\frac{1-w}{2}a^2, & 0\leq w<1,\\ 0, & w\geq 1.\end{cases}\end{aligned} \tag{11}$$

C. Convergence Analysis

In this subsection, we analyze the convergence behavior of REIT-HQ. Since $\boldsymbol{a}$ is updated at each iteration, we discuss the following two cases [22].

Update a: In $\mathcal{H}(\Delta\boldsymbol{\rho},\boldsymbol{W})$, $\mathcal{L}_a(\boldsymbol{w})$ is the only component related to $\boldsymbol{a}$. Based on (2), we take the partial derivative of $\mathcal{L}_a(w_{i,i})$ w.r.t. a

$$\frac{\partial\mathcal{L}_a(w_{i,i})}{\partial a}=\begin{cases}a, & w_{i,i}=0,\\ 0, & w_{i,i}=1.\end{cases} \tag{12}$$

Subsequently, we derive

$$\frac{\partial\mathcal{H}}{\partial a}=\frac{\partial\sum\mathcal{L}_a(w_{i,i})}{\partial a}=\sum\frac{\partial\mathcal{L}_a(w_{i,i})}{\partial a}\geq 0. \tag{13}$$

Thus, $\mathcal{H}(\Delta\boldsymbol{\rho},\boldsymbol{W})$ is monotonically non-decreasing w.r.t. a. As the updating rule in Section III-A makes a non-increasing, $\mathcal{H}(\Delta\boldsymbol{\rho},\boldsymbol{W})$ is monotonically non-increasing when a is updated.

Update $\{\Delta\boldsymbol{\rho},\boldsymbol{W}\}$: With a fixed a^{k+1}, as $\Delta\boldsymbol{\rho}^{k+1}$ and $\boldsymbol{W}^{k+1}$ are the optimal solution of (4a) and (4b), respectively, the following inequality must hold

$$\begin{aligned}&\mathcal{H}\left(\Delta\boldsymbol{\rho}^{k+1},\boldsymbol{W}^{k+1}\right)\\ &=\frac{1}{2}\|\sqrt{\boldsymbol{W}^{k+1}}\left(\Delta\boldsymbol{v}-\boldsymbol{J}\Delta\boldsymbol{\rho}^{k+1}\right)\|_2^2+\mathcal{L}_a\left(\boldsymbol{W}^{k+1}\right)\\ &\quad+\lambda\|\sqrt{\boldsymbol{Q}}\Delta\boldsymbol{\rho}^{k+1}\|_2^2\\ &\leq\frac{1}{2}\|\sqrt{\boldsymbol{W}^{k}}\left(\Delta\boldsymbol{v}-\boldsymbol{J}\Delta\boldsymbol{\rho}^{k+1}\right)\|_2^2+\mathcal{L}_a\left(\boldsymbol{W}^{k}\right)\\ &\quad+\lambda\|\sqrt{\boldsymbol{Q}}\Delta\boldsymbol{\rho}^{k+1}\|_2^2\\ &\leq\frac{1}{2}\|\sqrt{\boldsymbol{W}^{k}}\left(\Delta\boldsymbol{v}-\boldsymbol{J}\Delta\boldsymbol{\rho}^{k}\right)\|_2^2+\mathcal{L}_a\left(\boldsymbol{W}^{k}\right)\\ &\quad+\lambda\|\sqrt{\boldsymbol{Q}}\Delta\boldsymbol{\rho}^{k}\|_2^2\\ &=\mathcal{H}\left(\Delta\boldsymbol{\rho}^{k},\boldsymbol{W}^{k}\right).\end{aligned} \tag{14}$$

That is, $\{\mathcal{H}(\Delta\boldsymbol{\rho}^k,\boldsymbol{W}^k)\}$ is monotonically non-increasing. In addition, as $\mathcal{L}_a(\cdot)\geq 0$, $\{\mathcal{H}(\Delta\boldsymbol{\rho}^k,\boldsymbol{W}^k)\}$ is low bounded. Therefore, $\{\mathcal{H}(\Delta\boldsymbol{\rho}^k,\boldsymbol{W}^k)\}$ generated by Algorithm 1 is convergent.

D. Computational Complexity

The computational complexity for updating $\Delta\boldsymbol{\rho}^{k+1}$ is $\mathcal{O}(mn^2+n^3)$. Additionally, the complexity for computing $\boldsymbol{W}^{k+1}$ is $\mathcal{O}(mn+n)$. Therefore, the overall computational complexity is $\mathcal{O}(K(mn^2+n^3))$ with K iterations.

IV. EXPERIMENTAL RESULTS

In this section, the experimental settings, measurement index, and results are included as follows.

A. Measurement Setup

In this letter, we evaluate the suggested method using synthetic, resistor-net, and clinical data, where the collection equipment is the VenTom-100, Medias, Suzhou, China. Specifically, based on the CT image in the fourth intercostal location of a male thorax, a finite element model is established by Netgen software, which consists of 10, 171 triangular finite elements. Then, its 16 electrodes, each with a 10 mm diameter, are evenly set on the surface of the thorax based on the positions of the sternum and spine. Subsequently, the opposite current driving-adjacent voltage measurement mode is applied to perform EIT simulation [6], [7]. It is worth mentioning that the impulsive noise of resistor-net and clinical data are caused by the poor electrode contact and patient movement, respectively.

B. Measurement Index

We evaluate the reconstructed EIT images using four metrics, namely, the relative error (RE), correlation coefficient (CC), structural similarity index (SSIM), and peak signal-to-noise ratio (PSNR) [18]. Additionally, the reconstructed EIT images are assessed using four clinical indices, i.e., the center of ventilation (CoV) [27], global inhomogeneity (GI) [28], ventral-to-dorsal side ratio (V/D), and right-to-left lung ratio (R/L) [29]. The quality of the EIT images is compared by evaluating the images reconstructed using normal boundary voltages versus those rebuilt with corrupted boundary voltages. For example, $\text{CoV}_{\text{error}}=|\text{CoV}_{\boldsymbol{R}}-\text{CoV}_{\boldsymbol{R}^*}|$, where $\boldsymbol{R}^*$ represents the reconstructed EIT image based on the corrupted boundary voltages and $\boldsymbol{R}$ denotes the reference image.

C. Results

Parameter Investigation: We first investigate the influence of η on the imaging performance using the synthetic data generated from a finite element model. Specifically, we add impulsive noise to the 25-th channel of the EIT boundary voltage at intensities that scale the normal entry value by factors of $1,\ldots,9,10,20,\ldots,100$, resulting in 19 noise levels. Fig. 1 shows the impact of noise intensity and η on the reconstructed EIT images. It is seen that REs decrease and then increase with η increasing, when the impulsive noise level is fixed. Similarly,

TABLE I
EVALUATION INDICES BY DIFFERENT ALGORITHMS ON RESISTOR-NET AND CLINICAL DATA 1

Data Set	Method	RE	CC	SSIM	PSNR	$\mathrm{CoV}_{\mathrm{error}}$	$\mathrm{GI}_{\mathrm{error}}$	$\mathrm{V/D}_{\mathrm{error}}$	$\mathrm{R/L}_{\mathrm{error}}$
Resistor-net data	ℓ_2-EIT	1.41	-0.06	0.24	39.17	3.91	0.37	0.40	4.80
	ℓ_1-EIT	1.49	0.63	0.58	40.43	1.04	0.19	0.14	**0.001**
	NOSER	1.57	-0.01	0.13	39.12	26.53	67.78	1.91	2.26
	REIT-HQ	**0.42**	**0.96**	**0.78**	**52.51**	**0.38**	**0.14**	**0.05**	0.42
Clinical data 1	ℓ_2-EIT	1.52	-0.27	0.35	37.86	3.03	1.36	0.24	0.23
	ℓ_1-EIT	1.30	0.03	0.23	39.19	0.59	0.23	0.08	1.61
	NOSER	1.60	0.02	0.25	38.78	4.46	28.54	0.42	3.06
	REIT-HQ	**0.12**	**0.99**	**0.93**	**59.18**	**0.31**	**0.02**	**0.04**	**0.08**

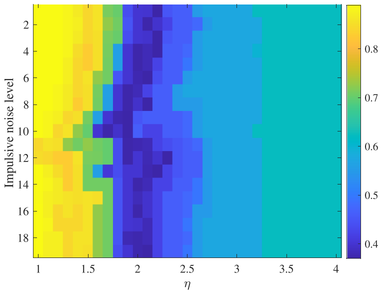

Fig. 1. Impulsive noise level versus η with synthetic data.

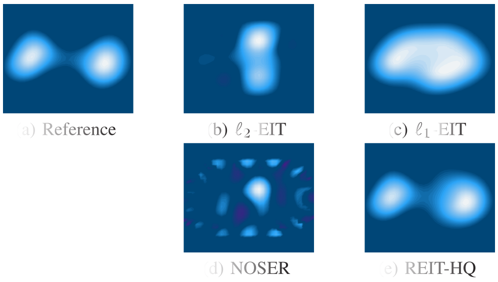
(a) Reference
(b) ℓ_2-EIT
(c) ℓ_1-EIT
(d) NOSER
(e) REIT-HQ

Fig. 2. EIT images reconstructed by different algorithms on resistor-net data. (a) Reference. (b) ℓ_2-EIT. (c) ℓ_1-EIT. (d) NOSER. (e) REIT-HQ.

REs have the same trend for impulsive noise level with a small η value.

Resistor-net Data: Then, we compare the suggested algorithm with ℓ_2 -EIT [30], ℓ_1-EIT [21], and NOSER [13] using the resistor-net data. We disconnect electrodes to model the scenario, where the electrode falls off due to body movement. The experimental results are presented in Fig. 2. It is seen that the ℓ_2-EIT and NOSER fail to reconstruct an accurate EIT image, and ℓ_1-EIT generates distorted pulmonary images with artificial artifacts. In contrast, the proposed algorithm successfully reconstructs the bilateral lung structures with enhanced anatomical fidelity, which closely matches the reference EIT image. Furthermore, the evaluation indices of the different algorithms on resistor-net data are shown in Table I.

Clinical Data: We further conduct a comparison using different clinical data. Figs. 3 and 4 display the visual results. It is evident that the EIT image reconstructed by the suggested algorithm closely matches the reference EIT image. In contrast, the competing algorithms fail to rebuild an accurate EIT image. Moreover, the evaluation metrics of the different algorithms are tabulated in Table I. It is seen that the proposed method outperforms the ℓ_2-EIT, ℓ_1-EIT, and NOSER. Besides, the computational efficiency by different algorithms on the clinical data 1 is shown in Table II. These results validate the clinical applicability of our approach in handling dynamic electrode contact variations during pulmonary function monitoring.

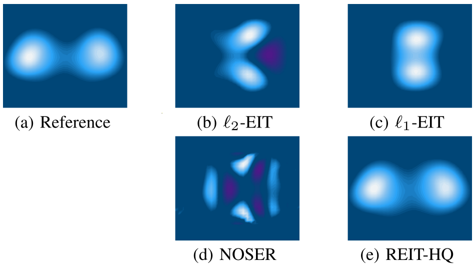
(a) Reference
(b) ℓ_2-EIT
(c) ℓ_1-EIT
(d) NOSER
(e) REIT-HQ

Fig. 3. EIT images reconstructed by different algorithms on clinical data 1. (a) Reference. (b) ℓ_2-EIT. (c) ℓ_1-EIT. (d) NOSER. (e) REIT-HQ.

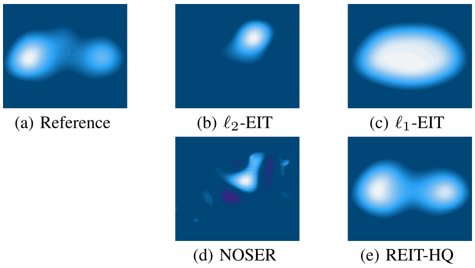
(a) Reference
(b) ℓ_2-EIT
(c) ℓ_1-EIT
(d) NOSER
(e) REIT-HQ

Fig. 4. EIT images reconstructed by different algorithms on clinical data 2. (a) Reference. (b) ℓ_2-EIT. (c) ℓ_1-EIT. (d) NOSER. (e) REIT-HQ.

TABLE II
COMPUTATIONAL EFFICIENCY OF DIFFERENT ALGORITHMS ON CLINICAL DATA 1

	ℓ_2-EIT	ℓ_1-EIT	NOSER	REIT-HQ
Per-iteration runtime (s)	–	0.0072	–	0.0075
Total execution time (s)	0.0051	1.1155	0.0054	0.0598
Iterations to converge	–	156	–	8

Note: "–" indicates non-iterative methods.

V. CONCLUSION

In this letter, we propose a robust EIT method to improve imaging performance in the presence of impulsive noise. Specifically, we introduce a regularization term for the weight matrix to resist outliers. Then, we formulate the imaging task as the HQ optimization problem with two variables that is efficiently solved using the AM method. Additionally, we design a MAD based confidence interval to identify the outlier-contaminated channels. Furthermore, the convergence property and computational complexity of the suggested approach are analyzed. Experimental results demonstrate that our method attains better performance than the competing algorithms with impulsive noise. However, the performance of our method deteriorates when the proportion of outlier-contaminated channels exceeds 50%, which is caused by the breakdown point of the MAD method.

REFERENCES

[1] M. Bodenstein, M. David, and K. Markstaller, “Principles of electrical impedance tomography and its clinical application,” *Crit. Care Med.*, vol. 37, pp. 713–724, Feb. 2009.

[2] T. Pengpan, N. Smith, W. Qiu, A. Yao, C. Mitchell, and M. Soleimani, “A motion-compensated cone-beam CT using electrical impedance tomography imaging,” *Physiol. Meas.*, vol. 32, Nov. 2010, Art. no. 19.

[3] Y. Gao et al., “Feasibility of 3D-EIT in identifying lung perfusion defect and v/q mismatch in a patient with VA-ECMO,” *Crit. Care*, vol. 28, Mar. 2024, Art. no. 90.

[4] T. N. Tallman and D. J. Smyl, “Structural health and condition monitoring via electrical impedance tomography in self-sensing materials: A review,” *Smart Mater. Structures*, vol. 29, Jun. 2020, Art. no. 123001.

[5] M. Shen et al., “Image reconstruction in open-EIT by combining inversion mapping and sparse contour representation,” *IEEE Trans. Instrum. Meas.*, vol. 73, 2024, Art. no. 4502209.

[6] X.-P. Li et al., “Robust electrical impedance tomography for respiratory monitoring,” *IEEE Trans. Instrum. Meas.*, vol. 74, 2025, Art. no. 4013112.

[7] L. Yang, M. Dai, S. Li, H. Wang, X. Cao, and Z. Zhao, “Real-time assessment of global and regional lung ventilation in the anti-gravity straining maneuver using electrical impedance tomography,” *Comput. Biol. Med.*, vol. 135, Aug. 2021, Art. no. 104592.

[8] R. Ribeiro De Santis Santiago et al., “Lung imaging acquisition with electrical impedance tomography: Tackling common pitfalls,” *Anesthesiology*, vol. 139, pp. 329–341, Apr. 2023.

[9] Y. Wu, F. F. Hanzaee, D. Jiang, R. H. Bayford, and A. Demosthenous, “Electrical impedance tomography for biomedical applications: Circuits and systems review,” *IEEE Open J. Circuits Syst.*, vol. 2, pp. 380–397, 2021.

[10] A. Roy and U. Satija, “RS-2-BP: A unified deep learning framework for deriving EIT-based breathing patterns from respiratory sounds,” *IEEE Signal Process. Lett.*, vol. 31, pp. 2785–2789, 2024.

[11] C. Panigrahy, A. Seal, and N. K. Mahato, “MRI and SPECT image fusion using a weighted parameter adaptive dual channel PCNN,” *IEEE Signal Process. Lett.*, vol. 27, pp. 690–694, 2020.

[12] S. R. Dubey, S. K. Singh, and R. K. Singh, “Local diagonal extrema pattern: A new and efficient feature descriptor for CT image retrieval,” *IEEE Signal Process. Lett.*, vol. 22, no. 9, pp. 1215–1219, Sep. 2015.

[13] M. Cheney, D. Isaacson, J. C. Newell, S. Simske, and J. Goble, “NOSER: An algorithm for solving the inverse conductivity problem,” *Int. J. Imag. Syst. Technol.*, vol. 2, pp. 66–75, Aug. 1990.

[14] A. Adler et al., “GREIT: A unified approach to 2D linear EIT reconstruction of lung images,” *Physiol. Meas.*, vol. 30, Jun. 2009, Art. no. S35.

[15] S. Liu, J. Jia, Y. D. Zhang, and Y. Yang, “Image reconstruction in electrical impedance tomography based on structure-aware sparse Bayesian learning,” *IEEE Trans. Med. Imag.*, vol. 37, no. 9, pp. 2090–2102, Sep. 2018.

[16] S. Liu, H. Wu, Y. Huang, Y. Yang, and J. Jia, “Accelerated structure-aware sparse Bayesian learning for three-dimensional electrical impedance tomography,” *IEEE Trans. Ind. Informat.*, vol. 15, no. 9, pp. 5033–5041, Sep. 2019.

[17] S. Liu, Y. Huang, H. Wu, C. Tan, and J. Jia, “Efficient multitask structure-aware sparse Bayesian learning for frequency-difference electrical impedance tomography,” *IEEE Trans. Ind. Informat.*, vol. 17, no. 1, pp. 463–472, Jan. 2021.

[18] D. Liu, J. Wang, Q. Shan, D. Smyl, J. Deng, and J. Du, “DeepEIT: Deep image prior enabled electrical impedance tomography,” *IEEE Trans. Pattern Anal. Mach. Intell.*, vol. 45, no. 8, pp. 9627–9638, Aug. 2023.

[19] X. Yang, Y. Zhang, H. Chen, G. Ma, and X. Wang, “A two-stage imaging framework combining CNN and physics-informed neural networks for full-inverse tomography: A case study in electrical impedance tomography (EIT),” *IEEE Signal Process. Lett.*, vol. 32, pp. 1096–1100, 2025.

[20] Y. Shi, Z. Yang, F. Xie, S. Ren, and S. Xu, “The research progress of electrical impedance tomography for lung monitoring,” *Front. Bioeng. Biotechnol.*, vol. 9, Oct. 2021, Art. no. 726652.

[21] A. Borsic and A. Adler, “A primal–dual interior-point framework for using the ℓ_1 or ℓ_2-norm on the data and regularization terms of inverse problems,” *Inverse Problems*, vol. 28, Aug. 2012, Art. no. 95011.

[22] Z. -Y. Wang, X. P. Li, and H. C. So, “Robust matrix completion based on factorization and truncated-quadratic loss function,” *IEEE Trans. Circuits Syst. Video Technol.*, vol. 33, no. 4, pp. 1521–1534, Apr. 2023.

[23] B. Grychtol, W. R. B. Lionheart, M. Bodenstein, G. K. Wolf, and A. Adler, “Impact of model shape mismatch on reconstruction quality in electrical impedance tomography,” *IEEE Trans. Med. Imag.*, vol. 31, no. 9, pp. 1754–1760, Sep. 2012.

[24] L. Yang et al., “Regional ventilation distribution in healthy lungs: Can reference values be established for electrical impedance tomography parameters,” *Ann. Transl. Med.*, vol. 9, May 2021, Art. no. 789.

[25] X. P. Li, Z.-Y. Wang, Z.-L. Shi, H. C. So, and N. D. Sidiropoulos, “Robust tensor completion via capped Frobenius norm,” *IEEE Trans. Neural Netw. Learn. Syst.*, vol. 35, no. 7, pp. 9700–9712, Jul. 2024.

[26] X. P. Li, Z. Liu, Z.-L. Shi, and H. C. So, “MUSIC with capped Frobenius norm: Efficient robust direction-of-arrival estimator,” *IEEE Trans. Aerosp. Electron. Syst.*, vol. 59, no. 6, pp. 8090–8103, Dec. 2023.

[27] U. Auer, J. P. Schramel, Y. P. Moens, M. Mosing, and C. Braun, “Monitoring changes in distribution of pulmonary ventilation by functional electrical impedance tomography in anaesthetized ponies,” *Vet. Anaesth. Analg.*, vol. 46, pp. 200–208, Mar. 2019.

[28] Z. Zhao, D. Steinmann, I. Frerichs, J. Guttmann, and K. Möller, “PEEP titration guided by ventilation homogeneity: A feasibility study using electrical impedance tomography,” *Crit. Care*, vol. 14, pp. 1–8, Jan. 2010.

[29] Z. Xiao et al., “Regional ventilation distribution before and after laparoscopic lung parenchymal resection,” *Physiol. Meas.*, vol. 45, Jan. 2024, Art. no. 15004.

[30] B. Grychtol, B. Müller, and A. Adler, “3D EIT image reconstruction with GREIT,” *Physiol. Meas.*, vol. 37, May 2016, Art. no. 785.